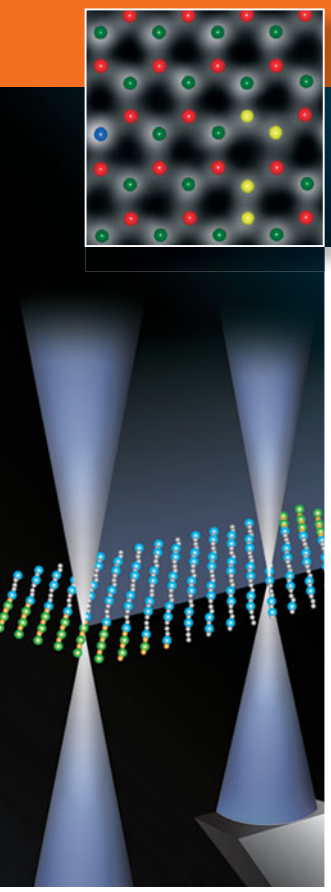

Spectroscopic imaging in electron microscopy

Stephen J. Pennycook and Christian Colliex, Guest Editors

In the scanning transmission electron microscope, multiple signals can be simultaneously collected, including the transmitted and scattered electron signals (bright field and annular dark field or Z-contrast images), along with spectroscopic signals such as inelastically scattered electrons and emitted photons. In the last few years, the successful development of aberration correctors for the electron microscope has transformed the field of electron microscopy, opening up new possibilities for correlating structure to functionality. Aberration correction not only allows for enhanced structural resolution with incident probes into the sub-Ångstrom range, but can also provide greater probe currents to facilitate mapping of intrinsically weak spectroscopic signals at the nanoscale or even the atomic level. In this issue of *MRS Bulletin*, we illustrate the power of the new generation of electron microscopes with a combination of imaging and spectroscopy. We show the mapping of elemental distributions at atomic resolution and also the mapping of electronic and optical properties at unprecedented spatial resolution, with applications ranging from graphene to plasmonic nanostructures, and oxide interfaces to biology.

A historic era for electron microscopy

The introduction of analytical devices within the columns of transmission electron microscopes (TEMs) has dramatically extended the field of information they can bring for the local exploration of materials and nanostructures. The primary electron beam in the electron microscope generates different signals when traveling through the specimen prepared as an ultrathin foil. The richness of the modern instruments operating in the scanning mode, in which a finely focused electron probe is rastered over the specimen (scanning transmission electron microscopy [STEM]), is to collect several complementary signals in parallel, giving birth to a multi-signal approach. A key success in recent years is to efficiently combine structural imaging and spectroscopic imaging in parallel in one electron microscope.[1–3]

Spectroscopic imaging is a general technique in which a multi-dimensional dataset is obtained, two of which would be spatial, while the third dimension would either be a full energy-loss spectrum,[4] or could equally well comprise an x-ray or cathodoluminescence (CL) spectrum, see **Figure 1**. The figure compares spectral imaging in STEM, where the energy dimension (E) is obtained in parallel and the spatial positions sequentially, with energy-filtered imaging in TEM (EFTEM), where the spatial image is obtained in parallel and the energy dependence sequentially (E_1 to E_2). It is important to note that in STEM, the spectrum image can be recorded simultaneously with other signals, such as the Z-contrast image obtained using an annular detector to collect scattered electrons, allowing pixel-by-pixel correlation of spectroscopic information with atomic structure. Spectroscopic imaging is valuable not only in electron microscopy but also in other microscopies, for example, scanning probe microscopy (SPM)[5] or 3D atom probe microanalysis.[6,7] It can also be used in higher dimensions, for example introducing a time dimension as in 4D electron microscopy,[8] or recording a diffraction pattern at each probe position in STEM or a hysteresis loop at each probe position in SPM.

Features in the electron energy-loss spectroscopy (EELS) spectrum carry information on the elemental composition through the appearance of characteristic core losses, as well as on the electronic properties through fine structure on the core loss edges and also from low-loss features. The origin and nature of these spectral features are discussed more fully in the contribution by Botton in this issue. It is essential to point out the direct correlation of these features with the position of the probe on the specimen, which can be defined with great accuracy relative to the structures to be analyzed. In **Figure 2**, this immediate correlation is demonstrated for different

Stephen J. Pennycook, Oak Ridge National Laboratory; pennycooksj@ornl.gov
Christian Colliex, Université Paris Sud, Orsay (France); colliex@lps.u-psud.fr
DOI: 10.1557/mrs.2011.332

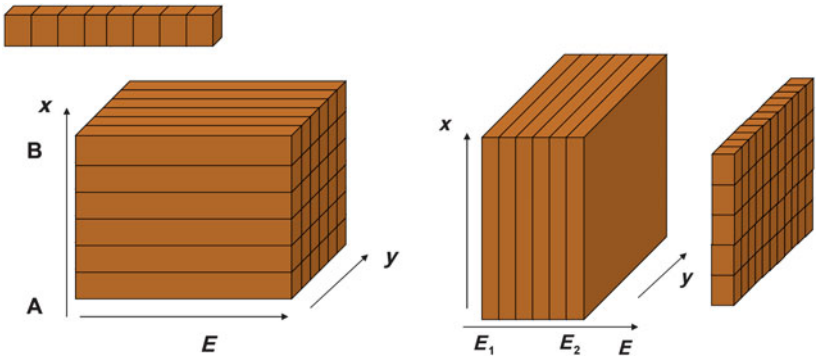

Figure 1. Schematic of the "data cube" obtained with spectroscopic imaging for the case of electron energy-loss spectroscopy, (left) scanning transmission electron microscope (STEM), (right) energy-filtered imaging in TEM. In the STEM, a line scan can be obtained by scanning in one dimension only (e.g., from A to B), with the energy loss data (E) being obtained in parallel. In the TEM, the spatial variation is obtained in parallel, while the energy loss is scanned in energy (e.g., from E_1 to E_2). (Adapted from Reference 4.)

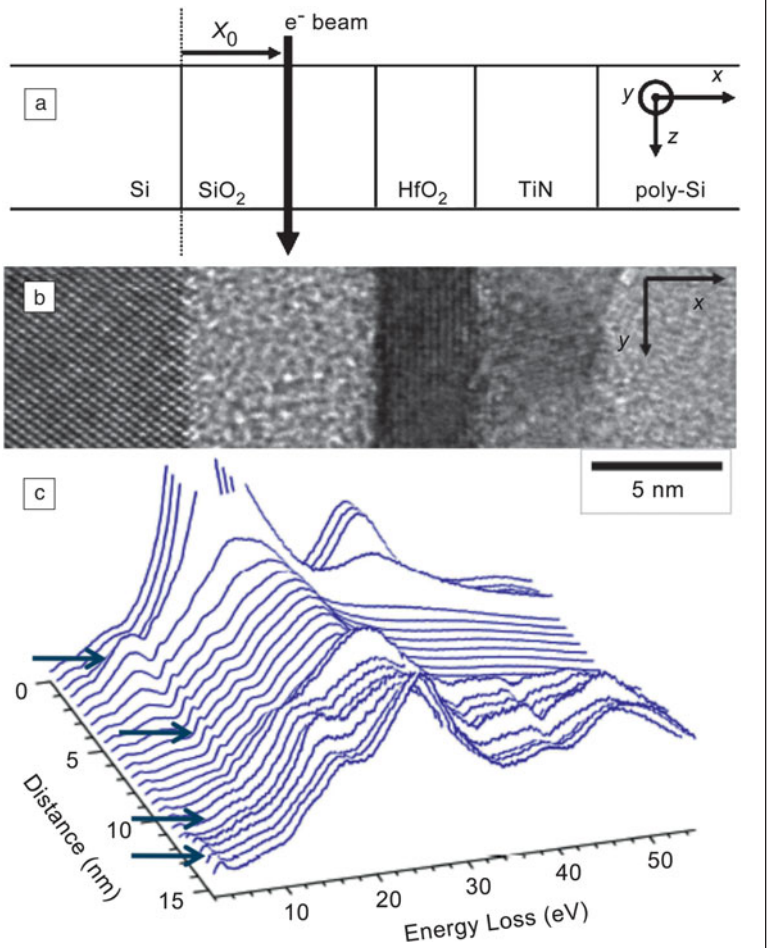

Figure 2. (a–b) Example of an electron energy-loss spectroscopy line spectrum across a sequence of layers from Si to TiN in a gate stack incorporating a thin layer of HfO_2. In (c), arrows from top to bottom identify an interface plasmon mode between Si and SiO_2, the bandgap in SiO_2, the bandgap in HfO_2, and an interface mode between HfO_2 and TiN. (Adapted from Reference 9.) Note: X_0, probe position along the scan direction (distance in (c)).

low-loss features appearing in a sequence of components within a semiconductor hetero-multilayer, showing changes in bandgaps and plasmon modes within individual layers and at their interfaces.

For most of the history of the electron microscope, its resolution has been limited by the aberrations of the primary imaging lens, the objective lens. Whereas in optical microscopy, resolutions comparable to the wavelength of light are readily achievable with high-quality components that minimize spherical and chromatic aberrations, in electron microscopy, the aberrations are intrinsic to the round magnetic field that is normally used as the objective lens, a fact first recognized in 1936 by Scherzer.[10] Since the aberrations are intrinsic, they cannot be avoided; however, they can be compensated for by higher order elements such as combinations of quadrupoles, hexapoles, or octapoles. An aberration corrector therefore becomes a highly complex set of electron-optical elements. Focusing such a device is beyond human ability and only became possible with computers, through iterative measurement and correction of aberrations.[11–13] Software is as important as hardware for achieving resolution, however, to the user, the complexity is largely hidden in the autotuning program, and day-to-day use is simpler than it was before aberration correction.

Today, correction of aberrations is typically achieved up to and including the fifth order (see References 14 and 15 for more details), and the resolution of the STEM has steadily improved,[16–20] recently surpassing 0.5 Å.[21,22] Both in STEM and in TEM, aberration correction has yielded dramatic new views of materials. For example, in ferroelectrics, it is now possible to directly map the displacements causing polarization and the octahedral tilts of the oxygen sublattice across interfaces and domain boundaries.[23–28] It has thus become possible to visualize point defect configurations inside materials,[29–32] even to identify individual light atoms in monolayer boron nitride (BN) and graphene based on their intensity in a Z-contrast image.[33,34] An example of the imaging of C and O impurities in monolayer BN is shown in **Figure 3**, where it can be seen that the O atoms always occupy the N sites, whereas the C atoms always substitute for a BN pair.

The benefits of aberration correction are at least as great for spectroscopic imaging; however, they are somewhat different. In many cases, such as the detection of x-rays, inner shell energy-loss events, or CL, the signals are usually much weaker than the standard imaging signals based on transmitted/scattered electrons. So, rather than aiming for the

https://doi.org/10.1557/mrs.2011.332 Published online by Cambridge University Press

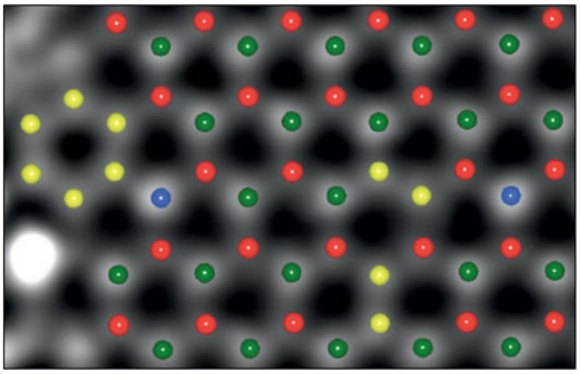

Figure 3. Z-contrast image of monolayer boron nitride with superimposed model structure. The image was obtained on a Nion UltraSTEM instrument operating at 60 kV to avoid knock-on damage and has been processed to remove noise and probe tail effects. Atomic identities were assigned based on image intensity, and the model relaxed using density functional theory. Red, B; green, N; yellow, C; and blue, O. The B–N separation is 1.45 Å. (Reproduced with permission from Reference 33.)

smallest probe, a larger probe is typically used with increased beam current to give better signal-to-noise ratios. In this case, as shown in **Figure 4**, aberration correction can lead to huge gains. For example, the fifth-order corrected microscope can generate the same size probe as the uncorrected version but with over 500 times as much current. To achieve that current in the uncorrected case would require the probe diameter to be increased more than five times.

Thus aberration correction opens a new regime for high spatial resolution spectroscopic imaging. In addition, post-specimen optics in the aberration-corrected microscope columns have also been improved, and EELS can often be performed with nearly 100% collection efficiency in the STEM, compared to the previous typical value of only 25%. The result is that for the first time, efficient, two-dimensional, elemental maps can be obtained from core loss signals with atomic resolution.[35,36] An example of the spectroscopic imaging of GaAs is shown in **Figure 5**, where the columns of Ga and As can be imaged individually. The figure also shows a composite signal in which the different elements are shown in different colors. This is a useful technique to show compositional variations.

The large data sets acquired with spectrum imaging invite image processing methods to reduce the noise and extract meaningful information. Popular methods include multivariate statistical analysis,[38,39] such as principal component analysis and multiple least squares fitting of EELS data. An example of the latter is shown in **Figure 6**, applied to a $SrTiO_3$/(La,Sr)MnO_3/$BiFeO_3$(STO/LSMO/BFO) interface. Here the spectra of the three different materials taken far from the interface are used as reference spectra to analyze the region close to the interface. In the core-loss regime (35 to 125 eV, with edges characteristic of atomic species), the three layers are easily distinguished, but in the low-loss regime (5 to 35 eV, representing interband and collective excitations of the compound), a region of BFO approximately 2 nm wide shows a significant residual in the χ^2 (goodness of fit) map. This indicates that the dielectric constant is anomolous in this region of the specimen. Interestingly, this is precisely the region where the tilts of the FeO_6 octahedra are perturbed from their bulk values due to the influence of the

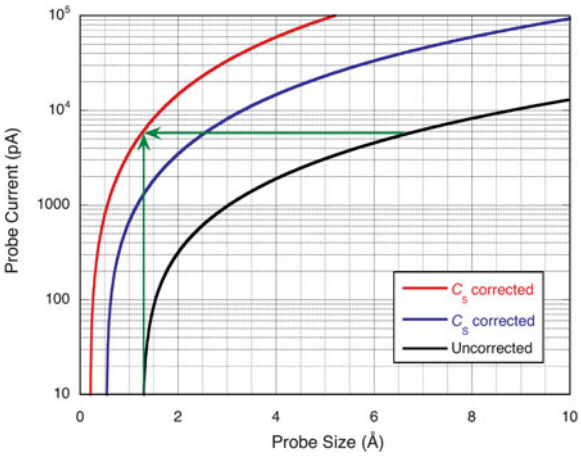

Figure 4. Plot of probe current versus probe size before aberration correction (black) and after correction of aberrations up to third-order (blue, C_s) and fifth-order (red, C_5). Green arrows highlight the increased current in the aberration corrected probe or the improved spatial resolution that can be obtained.

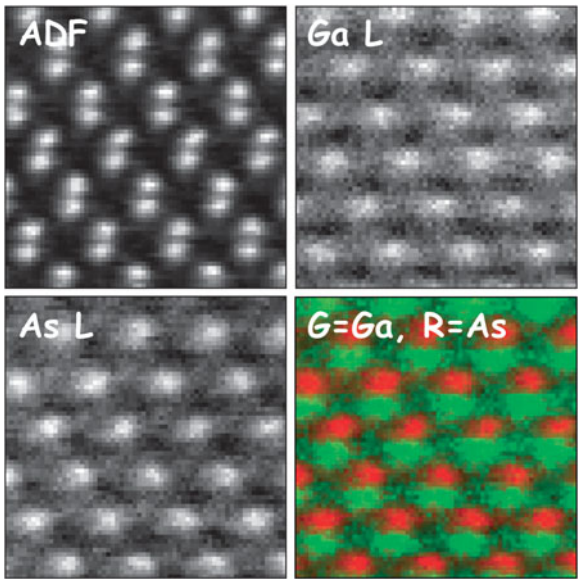

Figure 5. Spectroscopic imaging of GaAs in the ⟨110⟩ projection comparing the Z-contrast image to the Ga L and As L spectroscopic images, obtained on a Nion UltraSTEM with a fifth-order aberration corrector operating at 100 kV. Images are 64 x 64 pixels, with a collection time of 0.02 s/pixel and a beam current of approximately 100 pA, after noise reduction by principal component analysis.[37] The Ga–As separation is 1.41 Å. Note: ADF, annular dark field. Reproduced with permission from Reference 61.

https://doi.org/10.1557/mrs.2011.332 Published online by Cambridge University Press

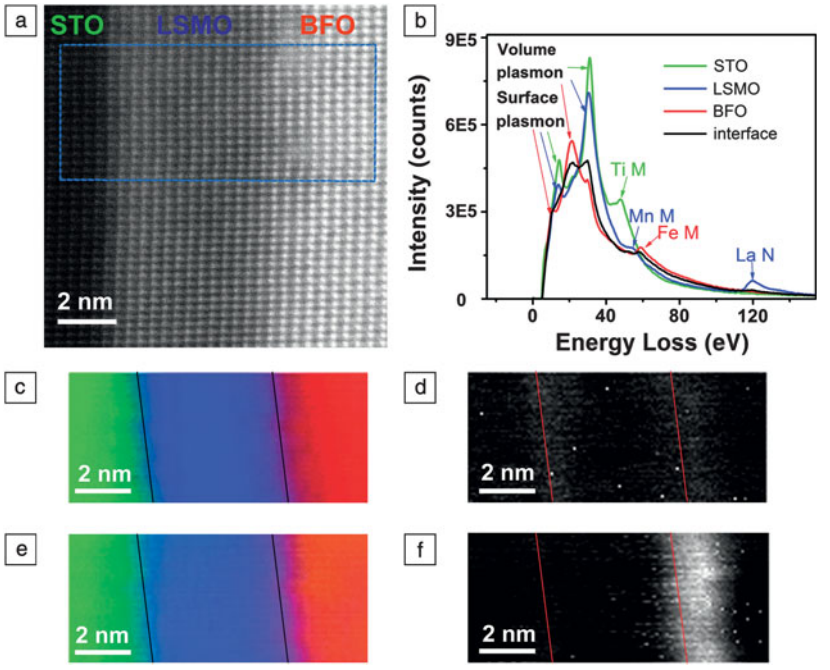

Figure 6. Low loss electron energy-loss spectroscopy imaging of the $SrTiO_3$/(La,Sr)MnO_3/$BiFeO_3$ (STO/LSMO/BFO) interface. (a) Imaging area; (b) representative spectra (after Fourier-log deconvolution) of the three components showing distinctive signatures and features; and (c–f) results of the multiple least squares fit of the image using BFO, LSMO, and STO spectra from (b) two energy ranges. Maps of the fit coefficients are color coded red, blue, and green for BFO, LSMO, and STO, respectively. In the core-loss range (35 to 125 eV), (c) a map of the fit coefficients identifies the three different materials in the three separate regions (shown in red, blue, and green), and (d) the goodness of fit χ^2 map shows minimal residual error. In the plasmonic range (5 to 35 eV), (e) the fit coefficient map correctly identifies the regions, but (f) the χ^2 map indicates a region of BFO approximately 2 nm wide that shows a poor fit, indicating an anomaly in dielectric response. Thin lines denote interface positions taken from a simultaneously acquired dark field image. (Reproduced from Reference 27.)

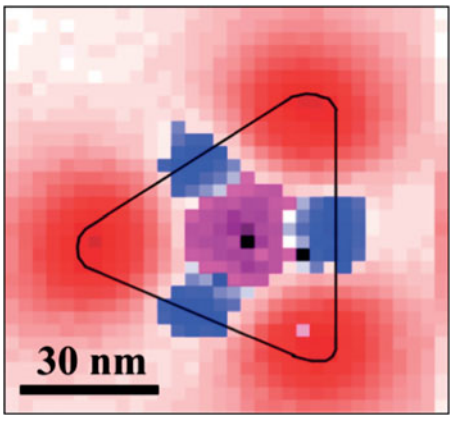

Figure 7. Absorbed real colors by a single silver nanoplatelet (a triangular-shaped prism of about 70 nm in side length and 8 to 10 nm in thickness), as deduced from a surface plasmon resonance map. This map exhibits peaks in the visible and near-visible spectral domain centered at different positions: it shows that, if illuminated by a white light photon beam, the red will be mostly absorbed at the tip, the blue at the edge, and the purple in the center of the metallic nanostructure. (Image courtesy of J. Nelayah, LPS Orsay.)

LSMO layer, which has no octahedral tilts. This region may also be the origin of the interfacial magnetic state observed at low temperature.[40] We thus see that there is a direct link between the detailed atomic structure and the electronic properties as revealed by EELS spectrum imaging, a good illustration of the kind of structure-property relationships that are accessible by aberration-corrected STEM.

An impact on materials science yet to be fully exploited

In this issue of *MRS Bulletin*, we explore a number of applications of spectrum imaging, EELS, CL, and x-rays, in materials science and biology. Botton gives an introduction to the technique of EELS, showing its sensitivity to the local density of states. He compares some of the instrumental aspects of STEM and TEM EELS, including spectrometers and monochromators, and gives a comparison with x-ray absorption spectroscopy. He shows how the near-edge fine structure allows the mapping of electronic structure in $BaTiO_3/SrTiO_3$ ferroelectrics and also in the area of multiferroic materials $BiFe_xCr_{1-x}O_3$ and reviews some recent examples of the investigation of charge ordering.

Varela et al. continue the theme of EELS spectrum imaging with applications from the field of complex oxides, resolving the mysterious properties of correlated oxide interfaces by revealing coupled structural distortions and associated changes in valence and band structure. The fine structure on the core edges of transition metal oxides has long been known to correlate with valence (i.e., the *d*-state occupancy)[41–46] but can now be mapped out with atomic resolution.[37,47–49] Varela et al. show how the fine structure reveals charge transfer across ferromagnetic/superconducting interfaces, giving rise to an orbital reconstruction and altered properties. Fine structure can also provide insights into the nature of colossal ionic conductivity in strained superlattices of STO and yttria-stabilized zirconia, Y_2O_3-ZrO_2 (YSZ); and in cobaltites, the fine structure can indicate the spin-state at atomic resolution.

Suenaga presents some of the highest spatial and spectral resolutions achieved to date for the core-level spectroscopy. Individual atoms and their valence state can be identified in nanostructured carbon materials, and localized electronic states can be detected at individual edge sites in graphene. The ability to study individual point defects, identify species, and examine their electronic structure is an excellent demonstration of the state of the art of the aberration-corrected STEM. Such investigations used to be the exclusive domain of the scanning tunneling microscope.

Another powerful recent application of EELS is in the field of plasmonics, wherein the optical energy range EELS can

https://doi.org/10.1557/mrs.2011.332 Published online by Cambridge University Press

provide much enhanced spatial resolution compared to light, opening up the possibility of investigating the fundamental optical properties of nanostructures at the nanoscale[50] (see **Figure 7**).

Kociak and García de Abajo describe an exciting combination of low-loss EELS and CL spectrum imaging that allows nanoscale mapping of plasmons, photons, and excitons, bringing the spatial resolution of EELS together with the spectral resolution of CL. They show a number of applications, including the investigation of quantum confinement in quantum wells only four monolayers thick, and the imaging of plasmon modes in plasmonic nanostructures. Such applications are bound to grow in the future as instrumental advances appear in the form of monochromators that will significantly enhance the EELS resolution in the optical range, and research in the areas of photonic bandgap materials, biosensors, photodetectors, and solar cells continues to grow.

X-ray detection has also recently achieved atomic resolution in the aberration-corrected STEM,[51–53] taking advantage of the ability to form small, high current probes. Chemical mapping with x-rays, as described in the article by Allen et al., is highly complementary to Z-contrast imaging and EELS, extending the range of elements that can be imaged spectroscopically, and generally involves high energy peaks that are localized at atomic sites. There also have been significant improvements in detector technology recently through increased detection efficiency and in avoiding the need for liquid nitrogen cooling, which often led to instabilities. X-rays can be collected simultaneously with the other signals, so why not use them? It seems likely that x-ray detection will become more popular for elemental mapping in the future.

Finally, the article by Aronova and Leapman describes the application of spectrum imaging to provide quantitative compositional information in biological materials on the nanometer scale. The authors show how EELS imaging can map the distributions of endogenous elements, such as phosphorus-containing nucleic acid in protein/nucleic acid complexes that regulate transcription of genes in cell nuclei, calcium in membrane-bound compartments that regulate cell signaling processes, and elements in metalloprotein complexes that regulate cytoplasmic levels of trace metals such as iron. They also show how EELS can be applied to measure exogenous elements that are introduced into cells in nanomedicine applications (e.g., gadolinium attached to dendrimer nanoparticle-based contrast agents used in magnetic resonance imaging). In addition, the authors describe how major chemical constituents, such as water and protein, can be mapped in frozen hydrated specimens by analyzing the EELS fine structure in spectrum images. They also show how EFTEM can be combined with electron tomography to provide quantitative three-dimensional elemental distributions within a volume, at a total electron dose that is comparable to that required to acquire a two-dimensional map. The authors include a discussion on the choice of image acquisition mode, EFTEM, or STEM, which depends on the type of application.

Summary

Aberration correction in the electron microscope has not only revolutionized structure imaging, but also spectroscopic imaging, bringing a combination of resolution and sensitivity that was unheard of just a few years ago. With electron energy-loss spectroscopy (EELS), we are now routinely able to map out electronic structure information at a sub-unit cell level, providing new insights into the origin of material properties. Such experimental capabilities call for better theoretical descriptions of EELS, which a few groups are pursuing.[54,55] For example, we need to go beyond the usual dipole approximation, as the scattering angles are no longer small. Also, the use of density functional theory to calculate the EELS fine structure usually assumes plane wave illumination, when in reality the electron beam has undergone multiple dynamical scattering.

In the future, we can look forward to continued instrumental developments, for example, use of a monochromator would dramatically improve spectral resolution for EELS.[56,57] Such developments would bring us closer to the ability to resolve vibrational states in materials, opening a new page for spectrum imaging. Since the depth of focus of an aberration-corrected probe is now typically smaller than a typical specimen thickness, we can anticipate probing three spatial dimensions with spectrum imaging. Some theoretical predictions of depth-resolved EELS already exist,[58] and there are potential benefits for true confocal geometry.[59] Time-resolved spectroscopic imaging will also exhibit fruitful developments in the continuation of the first studies realized by Zewail and his group,[60] and new exciting fields can be foreseen, such as the study of the non-linear optical response of nanostructures with incident fast electrons.

The electron microscope has evolved dramatically in the last several years, especially in its ability to map electronic and optical properties of materials with spectrum imaging. We hope that the articles in this issue of *MRS Bulletin* will present a glimpse of the breadth and depth of investigation that is available to further materials research.

Acknowledgments

S.J.P. acknowledges support from the U.S. Department of Energy, Basic Energy Sciences, Materials Sciences and Engineering Division. C.C. acknowledges the permanent support of CNRS, of Université Paris Sud and of EC programs, in particular the ESTEEM integrated infrastructure 026019.

References

1. C. Colliex, *J. Electron Microsc.* **60**, S161 (2011).
2. C. Colliex, N. Brun, A. Gloter, D. Imhoff, M. Kociak, K. March, C. Mory, O. Stephan, M. Tence, M. Walls, *Philos. Trans. R. Soc. London, Ser. A* **367**, 3845 (2009).
3. S.J. Pennycook, M. Varela, A.R. Lupini, M.P. Oxley, M.F. Chisholm, *J. Electron Microsc.* **58**, 87 (2009).
4. C. Jeanguillaume, C. Colliex, *Ultramicroscopy* **28**, 252 (1989).
5. S.V. Kalinin, B.J. Rodriguez, A.Y. Borisevich, A.P. Baddorf, N. Balke, H.J. Chang, L.Q. Chen, S. Choudhury, S. Jesse, P. Maksymovych, M.P. Nikiforov, S.J. Pennycook, *Adv. Mater.* **22**, 314 (2010).
6. D. Blavette, A. Bostel, J.M. Sarrau, B. Deconihout, A. Menand, *Nature* **363**, 432 (1993).
7. M.K. Miller, R.G. Forbes, *Mater. Charact.* **60**, 461 (2009).

https://doi.org/10.1557/mrs.2011.332 Published online by Cambridge University Press

8. A.H. Zewail, J.M. Thomas, *4D Electron Microscopy Imaging in Space and Time* (Imperial College Press, London, 2010).
9. M. Couillard, M. Kociak, O. Stephan, G.A. Botton, C. Colliex, *Phys. Rev. B* **76** (2007).
10. O. Scherzer, *Z. Phys.* **101**, 114 (1936).
11. M. Haider, S. Uhlemann, E. Schwan, H. Rose, B. Kabius, K. Urban, *Nature* **392**, 768 (1998).
12. O.L. Krivanek, N. Dellby, A.R. Lupini, *Ultramicroscopy* **78**, 1 (1999).
13. N. Dellby, O.L. Krivanek, P.D. Nellist, P.E. Batson, A.R. Lupini, *J. Electron Microsc.* **50**, 177 (2001).
14. S.J. Pennycook, P.D. Nellist, *Scanning Transmission Electron Microscopy: Imaging and Analysis* (Springer, New York, 2011).
15. R. Erni, *Aberration-Corrected Imaging in Transmission Electron Microscopy* (Imperial College Press, London, 2010).
16. P.D. Nellist, M.F. Chisholm, N. Dellby, O.L. Krivanek, M.F. Murfitt, Z.S. Szilagyi, A.R. Lupini, A. Borisevich, W.H. Sides, S.J. Pennycook, *Science* **305**, 1741 (2004).
17. P.E. Batson, N. Dellby, O.L. Krivanek, *Nature* **418**, 617 (2002).
18. H. Sawada, F. Hosokawai, T. Kaneyama, T. Ishizawa, M. Terao, M. Kawazoe, T. Sannomiya, T. Tomita, Y. Kondo, T. Tanaka, Y. Oshima, Y. Tanishiro, N. Yamamoto, K. Takayanagi, *Jpn. J. Appl. Phys.* **46**, L568 (2007).
19. C. Kisielowski, B. Freitag, M. Bischoff, H. van Lin, S. Lazar, G. Knippels, P. Tiemeijer, M. van der Stam, S. von Harrach, M. Stekelenburg, M. Haider, S. Uhlemann, H. Muller, P. Hartel, B. Kabius, D. Miller, I. Petrov, E.A. Olson, T. Donchev, E.A. Kenik, A.R. Lupini, J. Bentley, S.J. Pennycook, I.M. Anderson, A.M. Minor, A.K. Schmid, T. Duden, V. Radmilovic, Q.M. Ramasse, M. Watanabe, R. Erni, E.A. Stach, P. Denes, U. Dahmen, *Microsc. Microanal.* **14**, 469 (2008).
20. A.R. Lupini, A.Y. Borisevich, J.C. Idrobo, H.M. Christen, M. Biegalski, S.J. Pennycook, *Microsc. Microanal.* **15**, 441 (2009).
21. R. Erni, M.D. Rossell, C. Kisielowski, U. Dahmen, *Phys. Rev. Lett.* **102**, 096101 (2009).
22. H. Sawada, Y. Tanishiro, N. Ohashi, T. Tomita, F. Hosokawa, T. Kaneyama, Y. Kondo, K. Takayanagi, *J. Electron Microsc.* **58**, 357 (2009).
23. C.L. Jia, M. Lentzen, K. Urban, *Science* **299**, 870 (2003).
24. C.L. Jia, K. Urban, *Science* **303**, 2001 (2004).
25. K. Urban, *Science* **321**, 506 (2008).
26. A. Borisevich, O.S. Ovchinnikov, H.J. Chang, M.P. Oxley, P. Yu, J. Seidel, E.A. Eliseev, A.N. Morozovska, R. Ramesh, S.J. Pennycook, S.V. Kalinin, *ACS Nano* **4**, 6071 (2010).
27. A.Y. Borisevich, H.J. Chang, M. Huijben, M.P. Oxley, S. Okamoto, M.K. Niranjan, J.D. Burton, E.Y. Tsymbal, Y.H. Chu, P. Yu, R. Ramesh, S.V. Kalinin, S.J. Pennycook, *Phys. Rev. Lett.* **105**, 087204 (2010).
28. J. He, A. Borisevich, S.V. Kalinin, S.J. Pennycook, S.T. Pantelides, *Phys. Rev. Lett.* **105**, 227203 (2010).
29. S.H. Oh, K. van Benthem, S.I. Molina, A.Y. Borisevich, W.D. Luo, P. Werner, N.D. Zakharov, D. Kumar, S.T. Pantelides, S.J. Pennycook, *Nano Lett.* **8**, 1016 (2008).
30. D. Alloyeau, B. Freitag, S. Dag, L.W. Wang, C. Kisielowski, *Phys. Rev. B* **80**, 014114 (2009).
31. K. Kimoto, R. Xie, Y. Matsui, K. Ishizuka, N. Hirosaki, *Appl. Phys. Lett.* **94**, 041908 (2009).
32. S.Y. Chung, S.Y. Choi, T. Yamamoto, Y. Ikuhara, *Phys. Rev. Lett.* **100**, 125502 (2008).
33. O.L. Krivanek, M.F. Chisholm, V. Nicolosi, T.J. Pennycook, G.J. Corbin, N. Dellby, M.F. Murfitt, C.S. Own, Z.S. Szilagyi, M.P. Oxley, S.T. Pantelides, S.J. Pennycook, *Nature* **464**, 571 (2010).
34. O.L. Krivanek, N. Dellby, M.F. Murfitt, M.F. Chisholm, T.J. Pennycook, K. Suenaga, V. Nicolosi, *Ultramicroscopy* **110**, 935 (2010).
35. M. Bosman, V.J. Keast, J.L. Garcia-Munoz, A.J. D'Alfonso, S.D. Findlay, L.J. Allen, *Phys. Rev. Lett.* **99**, 086102 (2007).
36. D.A. Muller, L.F. Kourkoutis, M. Murfitt, J.H. Song, H.Y. Hwang, J. Silcox, N. Dellby, O.L. Krivanek, *Science* **319**, 1073 (2008).
37. M. Varela, M.P. Oxley, W. Luo, J. Tao, M. Watanabe, A.R. Lupini, S.T. Pantelides, S.J. Pennycook, *Phys. Rev. B* **79**, 085117 (2009).
38. N. Bonnet, N. Brun, C. Colliex, *Ultramicroscopy* **77**, 97 (1999).
39. M. Bosman, M. Watanabe, D.T.L. Alexander, V.J. Keast, *Ultramicroscopy* **106**, 1024 (2006).
40. P. Yu, J. Lee, S. Okamoto, M. Rossell, M. Huijben, C. Yang, Q. He, J. Zhang, S. Yang, M. Lee, Q. Ramasse, R. Erni, Y. Chu, D. Arena, C. Kao, L. Martin, R. Ramesh, *Phys. Rev. Lett.* **105**, 027201 (2010).
41. C. Colliex, P. Trebbia, *Ultramicroscopy* **9**, 259 (1982).
42. M. Isaacson, D. Johnson, *Ultramicroscopy* **1**, 33 (1975).
43. O.L. Krivanek, J.H. Paterson, *Ultramicroscopy* **32**, 313 (1990).
44. H. Kurata, C. Colliex, *Phys. Rev. B* **48**, 2102 (1993).
45. R.D. Leapman, L.A. Grunes, *Phys. Rev. Lett.* **45**, 397 (1980).
46. R.D. Leapman, L.A. Grunes, P.L. Fejes, *Phys. Rev. B* **26**, 614 (1982).
47. S. Van Aert, J. Verbeeck, R. Erni, S. Bals, M. Luysberg, D. Dyck, G. Tendeloo, *Ultramicroscopy* **109**, 1236 (2009).
48. L.F. Kourkoutis, H. Xin, T. Higuchi, Y. Hotta, J. Lee, Y. Hikita, D. Schlom, H. Hwang, D. Muller, *Philos. Mag.* **90**, 4731 (2010).
49. L. Gunawan, S. Lazar, O. Gautreau, C. Harnagea, A. Pignolet, G.A. Botton, *Appl. Phys. Lett.* **95**, 192902 (2009).
50. J. Nelayah, M. Kociak, O. Stephan, F.J. Garcia de Abajo, M. Tence, L. Henrard, D. Taverna, I. Pastoriza-Santos, L.M. Liz-Marzan, C. Colliex, *Nat. Phys.* **3**, 348 (2007).
51. M. Watanabe, *JEOL News* **45** (2010).
52. A.J. D'Alfonso, B. Freitag, D. Klenov, L.J. Allen, *Phys. Rev. B* **81**, 100101 (2010).
53. M.W. Chu, S.C. Liou, C.P. Chang, F.S. Choa, C.H. Chen, *Phys. Rev. Lett.* **104**, 196101 (2010).
54. C. Witte, S.D. Findlay, M.P. Oxley, J.J. Rehr, L.J. Allen, *Phys. Rev. B* **80**, 184108 (2009).
55. M. Prange, M.P. Oxley, S.J. Pennycook, S.T. Pantelides, in *Microscopy and Microanalysis 2011* (Microscopy and Microanalysis, Nashville, TN, 2011), vol. **17** (Suppl. 2), p. 808.
56. M. Haider, P. Hartel, H. Müller, *Philos. Trans. R. Soc. London, Ser. A* **367**, 3665 (2009).
57. O.L. Krivanek, J.P. Ursin, N.J. Bacon, G.J. Corbin, N. Dellby, P. Hrncirik, M.F. Murfitt, C.S. Own, Z.S. Szilagyi, *Philos. Trans. R. Soc. London, Ser. A* **367**, 3683 (2009).
58. A.J. D'Alfonso, S.D. Findlay, M.P. Oxley, S.J. Pennycook, K. van Benthem, L.J. Allen, *Ultramicroscopy* **108**, 17 (2007).
59. A.J. D'Alfonso, E.C. Cosgriff, S.D. Findlay, G. Behan, A.I. Kirkland, P.D. Nellist, L.J. Allen, *Ultramicroscopy* **108**, 1567 (2008).
60. F. Carbone, O.-H. Kwon, A.H. Zewail, *Science* **325**, 181 (2009).
61. S.J. Pennycook, M. Varela, *J. Electron Microsc.* **60**, S213 (2011). □

https://doi.org/10.1557/mrs.2011.332 Published online by Cambridge University Press